AIAA JOURNAL
Vol. 41, No. 9, September 2003

Inverse-Imaging Method for Detection of a Vortex in a Channel

Takao Suzuki* and Tim Colonius†
California Institute of Technology, Pasadena, California 91125

A simple vortex-imaging algorithm using a least-square method is considered. The position and the circulation of a vortex convected in a channel are identified from the time history of pressure at a limited number of points on the wall. The capabilities of the algorithm are demonstrated using two-dimensional direct numerical simulations. A few observer points on one side of the wall are sufficient to detect the position and the circulation of a compact vortex to a reasonable degree of accuracy. An advanced algorithm can even detect two nearby vortices to the same degree of accuracy. Because the algorithm assumes a point vortex solution, the accuracy of the detection deteriorates as the vorticity distribution spreads.

I. Introduction

INVERSE problems have been extensively investigated in many fields, such as solid mechanics, acoustics, electromagnetics, etc. However, only a very few inverse problems have been investigated in fluid mechanics[1–3] because of the nonlinearity of the governing equations. Although some structure identification techniques (e.g., the proper orthogonal decomposition[4] and the stochastic estimation[5]) based on surface pressure have been investigated,[6–8] these methodologies have focused on statistical approaches.

In this paper we develop a framework of a simple reconstruction algorithm using a least-square method for a vortex convected in a channel and generalize this idea to arbitrary flow configurations. From a limited number of observer points on the wall, the position and the circulation of a vortex are estimated. Hence, the database of the flowfield is not needed a priori. This type of noninvasive technique is potentially applicable to detect distinctive flow structures, such as streamwise vortices from trailing edges or on delta wings, separated bubbles inside a diffuser, rolling-up vortices in a cavity, etc. The inverse algorithm can also be relevant to active feedback flow control, in which the instantaneous flow pattern must be identified from a limited number of sensors. Thus, we expect that systematic study of inverse problems incorporating with feedback flow control or experimental techniques will bring us great benefit.

II. Reconstruction Process

A. Imaging a Single Vortex in a Channel

We consider a single point vortex convected in a channel and assume an ideal fluid (see Fig. 1 for the coordinate system). A limited number of observer points are distributed only on the upper wall ($y = 1$). The position and circulation of the vortex is to be detected only from the pressure time history at these points. The position in the horizontal direction can be easily identified from pressure deficit on the wall induced by the vortex. The difficulty is to determine the circulation and the height of the vortex.

For an ideal fluid the analytic solution to the forward problem can be found (cf., Saffman[9]). We define the physical domain as $z = x + iy$ and use a conformal mapping expressed by $\zeta = \exp[(\pi/2)z]$: We can map the channel into the first quadrant, and two pairs of counter-rotating vortices satisfy the nonpenetration boundary conditions in the ζ domain. After some calculation the convective velocity of the vortex in the physical domain can be given as a function of y_0:

$$u_c = (\Gamma/4)[1/\tan(\pi y_0)] \tag{1}$$

If the vortex approaches the upper wall, the induced velocity of the image vortex on the upper side becomes stronger so that the real vortex moves to the left, and vice versa. Thus, if the convective velocity can be estimated from the time-dependent pressure data, it can in turn be used to estimate the height of the vortex.

The pressure fluctuation on the wall caused by the vortex can be readily calculated using Bernoulli's equation:

$$p(\Gamma, x_0, y_0; x) = p_\infty - \frac{\rho\Gamma^2}{2}\left\{\left[\frac{\eta^2 \sin 2\theta}{(\eta^2+1)^2 - 4\eta^2 \sin^2\theta}\right]^2 + \frac{1}{2\tan 2\theta}\frac{\eta^2 \sin 2\theta}{(\eta^2+1)^2 - 4\eta^2 \sin^2\theta}\right\} \tag{2}$$

where p_∞ is the ambient pressure in the far field (assumed known), $\theta \equiv (\pi/2)y_0$, and $\eta \equiv \exp[(\pi/2)(x - x_0)]$. Subsequently, the derivative of the pressure with respect to time can be expressed as

$$\dot{p}(\Gamma, x_0, y_0; x) = \frac{\partial p}{\partial x_0}\frac{\mathrm{d}x_0}{\mathrm{d}t} = -\frac{\partial p}{\partial x}(u_\infty + u_c) \tag{3}$$

where u_∞ is the freestream velocity in the channel and u_c is given by Eq. (1). The strategy is to find the position and the circulation that best match Eqs. (2) and (3) simultaneously.

To evaluate this, we introduce a cost function of the least-square type:

$$J(t, \Gamma, x_0, y_0) = \sum_{m=1}^{N_m}\left[w_1(\Gamma, x_0, y_0; q)|p(\Gamma, x_0, y_0; x_m) - q(t, x_m)|^2 + w_2(\Gamma, x_0, y_0; \dot{q})|\dot{p}(\Gamma, x_0, y_0; x_m) - \dot{q}(t, x_m)|^2\right] \tag{4}$$

where N_m denotes the number of the observer points and x_m and $q(t, x_m)$ are the position and measured pressure for the mth observer, respectively. The first term in Eq. (4) mainly determines the horizontal coordinate x_0 and the second term the vertical coordinate y_0. In this study we simply set the weight functions w_1 and w_2 so that the relative errors from both terms are equal and they depend only on q and $\dot{q}$, respectively:

$$w_1(q) = \left[\sum_{m=1}^{N_m}|q(t, x_m) - p_\infty|^2\right]^{-1} \tag{5}$$

$$w_2(\dot{q}) = \left[\sum_{m=1}^{N_m}|\dot{q}(t, x_m)|^2\right]^{-1} \tag{6}$$

Received 30 September 2002; revision received 3 March 2003; accepted for publication 25 April 2003.

*Postdoctoral Scholar, Division of Engineering and Applied Science. Member AIAA.
†Associate Professor, Division of Engineering and Applied Science. Member AIAA.

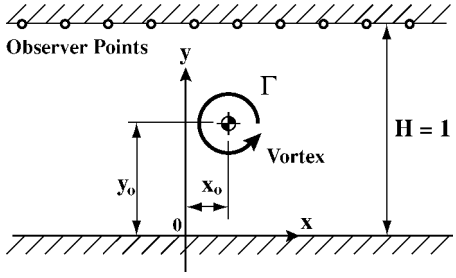

Fig. 1 Schematic of the model problem.

To minimize J, we differentiate it with respect to Γ. This must satisfy

$$\frac{\partial J}{\partial \Gamma}(t, \Gamma, x_0, y_0) = 2\sum_{m=1}^{N_m}\left[w_1\frac{\partial p}{\partial \Gamma}(p-q) + w_2\frac{\partial \dot{p}}{\partial \Gamma}(\dot{p}-\dot{q})\right]_m = 0 \tag{7}$$

where the subscript m indicates that the quantity is evaluated at the mth observer position. Equation (7) gives the estimated circulation Γ^* if the vortex is located at $(x, y) = (x_0, y_0)$. Substituting Γ^* into Eq. (4), we can compute the cost function at each point and map it on the (x_0, y_0) domain. Thus, we create a vortex image map on which the local minimum of $J(t, \Gamma^*, x_0, y_0)$ indicates the vortex position.

B. Imaging Multiple Vortices

If we directly apply this algorithm (called the single-vortex algorithm in this paper) to a flow with multiple vortices, the resultant image map can indicate the corresponding number of distinct local minima of the cost function. However, the accuracy of the detection is expected to drop significantly as the vortices become closer. In such a case we can construct the ideal solutions for multiple vortices and detect them simultaneously. For simplicity, we discuss an algorithm for two vortices below (called the double-vortex algorithm in this paper).

In what follows we use subscripts 1 and 2, referring to primary and secondary vortices, respectively. First, we create a preliminary image map to define the primary vortex using the single-vortex algorithm as just described. We then create an image map for the secondary vortex by minimizing the cost function with respect to Γ_1, x_1, y_1, and Γ_2:

$$\frac{\partial J}{\partial \Gamma_1}(\Gamma_1, x_1, y_1, \Gamma_2, x_2, y_2) = 2\sum_{m=1}^{N_m}\left[w_1\frac{\partial p}{\partial \Gamma_1}(p-q) + w_2\frac{\partial \dot{p}}{\partial \Gamma_1}(\dot{p}-\dot{q})\right]_m = 0 \tag{8}$$

$$\frac{\partial J}{\partial x_1}(\Gamma_1, x_1, y_1, \Gamma_2, x_2, y_2) = \cdots = 0 \tag{9}$$

$$\frac{\partial J}{\partial y_1}(\Gamma_1, x_1, y_1, \Gamma_2, x_2, y_2) = \cdots = 0 \tag{10}$$

$$\frac{\partial J}{\partial \Gamma_2}(\Gamma_1, x_1, y_1, \Gamma_2, x_2, y_2) = \cdots = 0 \tag{11}$$

where $p = p(\Gamma_1, x_1, y_1, \Gamma_2, x_2, y_2; x, y)$ and $\dot{p} = \dot{p}(\Gamma_1, x_1, y_1, \Gamma_2, x_2, y_2; x, y)$ are the solutions to the potential flow with two vortices and w_1 and w_2 are specified to be functions of only q and $\dot{q}$, respectively. Subsequently, we iteratively solve these simultaneous equations and map the optimized $J(\Gamma_1^*, x_1^*, y_1^*, \Gamma_2^*, x_2, y_2)$ on the (x_2, y_2) domain. As a consequence of the optimization, more accurate estimates are obtained for Γ_1, x_1, and y_1 than the preliminary estimates found from the single-vortex algorithm.

C. Imaging a Vortex Based on Approximated Solutions

When a vortex is convected in a curved flow, the potential solution cannot be expressed by a simple formula. In such cases we can approximate the potential solution by a family of simple functions with several parameters. As an example, we consider a curved channel in which the coordinate in the flow direction is given by ξ and that in the transverse direction by η (Fig. 2). From the preceding discussion we observe that the position of the pressure minimum approximately gives the ξ coordinate, and the width of this pressure deficit strongly depends on the η coordinate. In addition, as the circulation increases the pressure deficit enhances. From such observation suppose we model the exact solution on the upper wall using the following formula:

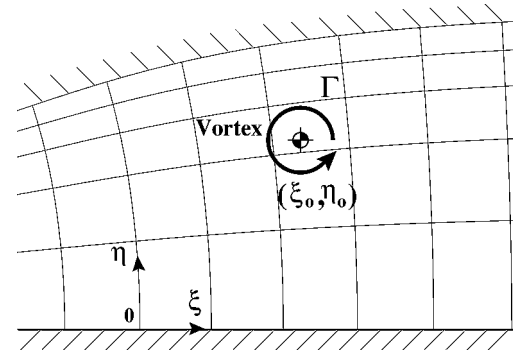

Fig. 2 Coordinate system in a curved channel.

$$\tilde{p}(a, b, c; \Gamma, \xi_0, \eta_0; \xi_m) \equiv \bar{p}(\xi_m) - \frac{a\Gamma^c}{b(1-\eta_0)}\exp\left[-\frac{(\xi_m-\xi_0)^2}{b^2(1-\eta_0)^2}\right] \tag{12}$$

where $\bar{p}(\xi_m)$ denotes the pressure for the mth observer when a vortex is absent.

Now, if the potential solutions with several different combinations of (Γ, ξ_0, η_0) are available from computation (the total number of the samples denoted by N_n), we can determine the coefficients a, b, and c by minimizing the following cost function:

$$\tilde{J}(a, b, c) \equiv \sum_{n=1}^{N_n}\varpi_n\sum_{m=1}^{N_m}|\tilde{p}(a, b, c; \Gamma_n, (\xi_0)_n, (\eta_0)_n; \xi_m, \eta_m) - p(\Gamma_n, (\xi_0)_n, (\eta_0)_n; \xi_m, \eta_m)|^2 \tag{13}$$

where p is again the potential solution and

$$\varpi_n \equiv \left\{\sum_{m=1}^{N_m}|p(\Gamma_n, (\xi_0)_n, (\eta_0)_n; \xi_m, \eta_m) - \bar{p}(\xi_m)|^2\right\}^{-1}$$

for convenience.

Similarly, the time derivative $\tilde{\dot{p}}$ could be approximated by some model function. In this study, however, assuming that the mapping function from the curvilinear coordinates (ξ, η) to the physical coordinates (x, y) is known, we use the same convective velocity derived in Eq. (1) and the relation (3) in the (ξ, η) domain. In addition, we assume that the freestream velocity [denoted by u_∞ in Eq. (3)] is aligned with an iso-η line. Determining a, b, and c, we can use $\tilde{p}$ and $\tilde{\dot{p}}$ instead of p and $\dot{p}$ and follow the same procedure to create vortex-image maps.

D. Estimator-Corrector

If we keep track of the vortex position and circulation over time, we can take the flow dynamics into account by using the information from the preceding time step; accordingly, we can suppress the random errors associated with the detection process. Defining the state vector to be $\boldsymbol{x} \equiv (\Gamma, x_0, y_0)^T$, $\boldsymbol{e}$ to be the error of $\boldsymbol{x}$, $\boldsymbol{u} \equiv \dot{\boldsymbol{x}}$ given from the potential solution, and $\delta\boldsymbol{u}$ to be the error of $\boldsymbol{u}$, we can express the governing equation at the time step $i+1$ to be

$$\boldsymbol{x}_{i+1} = \boldsymbol{x}_i + \boldsymbol{u}_i\Delta t \tag{14}$$

where $\boldsymbol{u}_i \equiv \boldsymbol{u}(\boldsymbol{x}_i)$ and the error associated with temporal discretization is neglected. The corresponding equation estimated via the observers can be expressed as

$$\boldsymbol{x}_{i+1} + \boldsymbol{e}_{i+1} = r[\boldsymbol{x}_i + \boldsymbol{e}_i + (\boldsymbol{u}_i + \delta\boldsymbol{u}_i)\Delta t] + (1-r)[\boldsymbol{x}_{i+1} + \boldsymbol{w}_{i+1}] \tag{15}$$

where $0 < r < 1$ and $\boldsymbol{w}_{i+1}$ denotes the random error associated with the inverse process at the time step $i+1$. Here, the first term gives the prediction based on the vortex dynamics, and the second term gives the detection from the inverse algorithm. From Eqs. (14) and (15) the recursive relation of the error term yields

$$\boldsymbol{e}_{i+1} = r\left(I + \Delta t \frac{\partial \boldsymbol{u}}{\partial \boldsymbol{x}}\right)\boldsymbol{e}_i + (1-r)\boldsymbol{w}_{i+1} \tag{16}$$

If $\boldsymbol{w}_i$ is independent and identical with the mean zero, the expectation of the error at the time step n yields

$$E\left[\boldsymbol{e}_n^2\right] = \left[\hat{r}^{2n} + (r-1)^2 \frac{\hat{r}^{2n} - 1}{\hat{r}^2 - 1}\right] E[\boldsymbol{w}^2] \tag{17}$$

where $E[\boldsymbol{e}_n^2] \equiv [(\delta\Gamma)_n^2, (\delta x_0)_n^2, (\delta y_0)_n^2]^T$ and $\hat{r} \equiv r \cdot \max[\text{eigenvalues of } (I + \Delta t\, \partial \boldsymbol{u}/\partial \boldsymbol{x})]$. Thus, as $n \to \infty$ we should choose r so that $\hat{r} < 1$ but close to unity. The deviation can be then suppressed as $E[\boldsymbol{e}_\infty^2] \approx (1-r)^2/(1-\hat{r}^2) E[\boldsymbol{w}^2]$.

E. Generalization of the Algorithm Using a Least-Square Method

The preceding idea can be generalized as follows: Suppose that the exact solution is given at the observer positions as $P_k(\alpha, \beta, \cdots; \boldsymbol{x}_m)$ and the corresponding measured data are available as $Q_k(\boldsymbol{x}_m)$. Here, the Greek letters $\alpha, \beta, \cdots$ denote the parameters that we wish to identify. In the first example they correspond to Γ, x_0, and y_0. The types of the data for P_k and Q_k are arbitrary; that is, they can be pressure, velocity, their derivatives, etc., and the subscript k denotes its type. In the preceding example $k = 1$ corresponds to pressure, and $k = 2$ its time derivative. Supposing N_k types of measured data are available, we can define the cost function as follows:

$$J(\alpha, \beta, \cdots) = \sum_{k=1}^{N_k} \left[w_k(\alpha, \beta, \cdots; Q_k) \times \sum_{m=1}^{N_m} |P_k(\alpha, \beta, \cdots; \boldsymbol{x}_m) - Q_k(\boldsymbol{x}_m)|^2 \right] \tag{18}$$

To minimize this cost function, we differentiate it with respect to each Greek parameter as follows:

$$\frac{\partial J}{\partial \alpha} = \sum_{k=1}^{N_k} \sum_{m=1}^{N_m} \left[2w_k \frac{\partial P_k}{\partial \alpha}(P_k - Q_k) + \frac{\partial w_k}{\partial \alpha}(P_k - Q_k)^2 \right]_m = 0 \tag{19}$$

$$\frac{\partial J}{\partial \beta} = \cdots = 0 \tag{20}$$

In the preceding example the second term vanishes as w_k is assumed independent of the Greek letters. If only a single object exists in the target domain, this algorithm might work faster. In many practical situations, however, J has several local minima; hence, we might want to map J onto a parameter domain. If two vortices exist relatively far apart, we set α to be Γ and map $J(\Gamma^*)$ onto the (x_0, y_0) domain. When two vortices are fairly close, we set $\alpha, \beta, \cdots$ to be Γ_1, x_1, x_2, and Γ_2 and map J onto the (x_2, y_2) domain or vice versa.

In a special case in which the solution is a linear function of a Greek parameter, we can make the algorithm simpler. Suppose that the exact solution has a form of $P_k(\alpha, \beta, \cdots; \boldsymbol{x}_m) = \alpha \hat{P}_k(\beta, \cdots; \boldsymbol{x}_m)$; accordingly, w_k is defined such that it is independent of α. From Eq. (19) α can be immediately given by

$$\alpha = \frac{\sum_{k=1}^{N_k} w_k \sum_{m=1}^{N_m} (\hat{P}_k Q_k)_m}{\sum_{k=1}^{N_k} w_k \sum_{m=1}^{N_m} (\hat{P}_k)_m^2} \tag{21}$$

The rest of the Greek parameters are determined as calculated in Eq. (20). In the preceding example, if $u_\infty \equiv 0$ we can use this algorithm by setting $\alpha \equiv \Gamma^2$ and assuming p_∞ to be given.

In many situations, however, we might not be able to readily obtain the exact solutions. In such cases the exact solution P_k can be approximated by a simpler function $\tilde{P}_k$ as mentioned before. First, we assume a family of functions $\tilde{P}_k$ with several parameters, $a, b, \cdots$ and determine them by optimizing a cost function, such as

$$\tilde{J}(a, b, \cdots) = \sum_{k=1}^{N_k} w_k \sum_{n=1}^{N_n} (\varpi_k)_n \sum_{m=1}^{N_m} |\tilde{P}_k(a, b, \cdots; \alpha_n, \beta_n, \cdots; \boldsymbol{x}_m) - P_k(\alpha_n, \beta_n, \cdots; \boldsymbol{x}_m)|^2 \tag{22}$$

It would be desirable to select the sampling parameters $\alpha_n, \beta_n, \cdots$ so that they efficiently span the target domain. After we find $a, b, \cdots$, which minimize Eq. (22), we use $\tilde{P}_k$ instead of P_k and follow the same algorithm.

III. Numerical Methods

A. Direct Numerical Simulation

To demonstrate the capabilities of the inverse algorithm, we performed direct numerical simulations (DNS) in two dimensions. We used a diffuser geometry as a vortex generator and artificially forced the boundary layer near the separation point to generate different sizes and distances of vortices.[10] We distributed observer points on the upper wall with approximately equal spacing in the x direction (Fig. 3). We used the observer points downstream for a straight channel problem and those in the upstream part for a curved channel problem. We imposed the nonslip boundary conditions on the upper wall and the symmetric conditions on the lower side. Further details regarding the numerical procedures can be found in Suzuki et al.[10]

To nondimensionalize the equations, the exit height h_2 is taken to be the length scale and the freestream velocity at the exit u_∞ to be the velocity scale. The area ratio was set to be $h_1/h_2 = 0.5$ (h_1 being the inlet height), the exit Reynolds number was $Re = 4 \times 10^3$, and the exit freestream Mach number was nearly incompressible ($M_\infty \approx 0.15$). The momentum thickness of the inlet laminar boundary layer was set to be $\delta_{b.l.} = 0.025$. The pressure data were sampled at the computation time step of $\Delta t = 1.5 \times 10^{-4}$. The ambient pressure p_∞ and the freestream convective velocity u_∞ were measured at $x = 4$ before vortices were convected and assumed to be given in the reconstruction process.

B. Inverse Algorithm

We tested the algorithms at a variety of conditions and created image maps. We iteratively solved Eq. (7) using the Newton method for the single-vortex algorithm or Eqs. (8–11) using the Newton–Raphson method for the double-vortex algorithm. Because the convergence of the Newton–Raphson method is quite sensitive to the initial values, they were chosen from the optimized values at 100 previous time steps, and this procedure was repeated over time. The resolution of the target domain was set to be $\Delta x = \Delta y = 0.01$ ($\Delta\xi = \Delta\eta = 0.01$ for the curved channel problem).

To validate the algorithm using an approximated function, we tried to detect a vortex also in a curved channel part. The diffuser shape is given by the following conformal mapping

$$z \equiv x + iy = \tfrac{3}{4}\{\zeta + 0.4400 \log[\cosh(0.7576\zeta)]\} \tag{23}$$

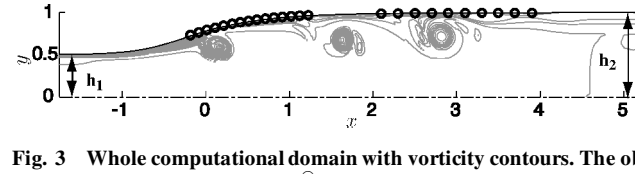

Fig. 3 Whole computational domain with vorticity contours. The observer points are denoted by ○. The group on the left-hand side (15 points) is on the curved part, and the right-hand side (10 points) is on the straight part.

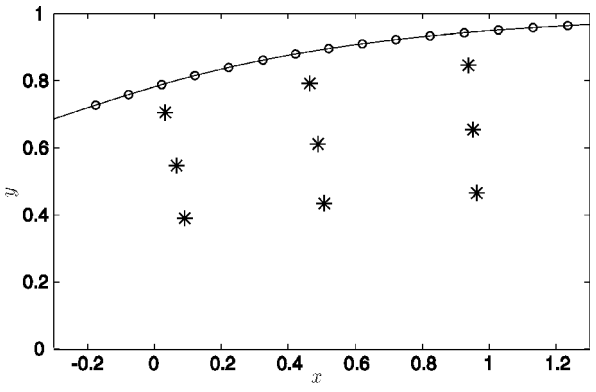

Fig. 4 Flow geometry in the curved channel: ∗, points where the samples of the potential solutions were taken and ○, 15 observer points, which were distributed with a spacing of approximately 0.1 in the x direction.

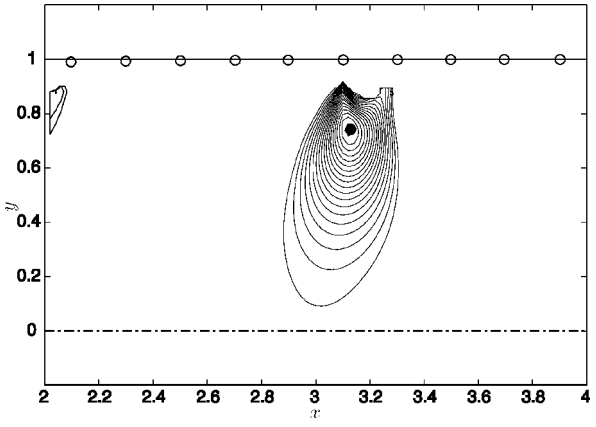

Fig. 5 Image map of a small vortex created using the single-vortex algorithm. Contours of $-J$ corresponding to Fig. 6 are drawn with the interval of $\Delta J = 0.05$: ●, detected position and ○, observer points. The cost function at the detected point is $J_{\min} = 0.886$.

where $\zeta \equiv \xi + i\eta$. Assuming this mapping function is known, we used a family of functions expressed in Eq. (12) for the ideal solution. To determine the coefficients a, b, and c, nine sample points (depicted in Fig. 4) times three values of circulations ($\Gamma = 0.333$, 0.667, and 1.333), that is, a total of 27 samples of the potential solutions for a point vortex, were solved, and the pressure profiles at the observer points were computed based on the unsteady Bernoulli's equation. These potential solutions were used in minimizing the cost function shown in Eq. (13), which gave $a = 1.98 \times 10^{-4}$, $b = 0.678$, and $c = 1.626$.

We also tested the estimator-corrector for two cases (one and two compact vortices). In both cases we used the single vortex algorithm to give the second term in Eq. (15) and set $r = 0.9$ for the estimator-corrector so that it satisfies $\hat{r} < 1$.

IV. Results and Discussion

A. Detection of Single Vortex in Straight Channel Based on the Potential Solution

First, we show the results of compact vortices detected using the single-vortex algorithm with 5, 10, and 20 observer points. Figures 5–8 depict image maps of one and two vortices and their comparisons between the detected vortex positions with 10 points and the vortex centroids computed from DNS superposed on the vorticity contours. They demonstrate that the position of the vortex is identified very well (within 0.03 in both examples). Even two vortices can be captured in a single map if they are sufficiently separated. Here, the vortex centroid and the circulation in DNS were calculated by defining the vortex region to be within a simple support up to 3% of the peak vorticity.

We can confirm the accuracy of detection from the trajectories of the vortex and the circulation in Figs. 9 and 10, respectively.

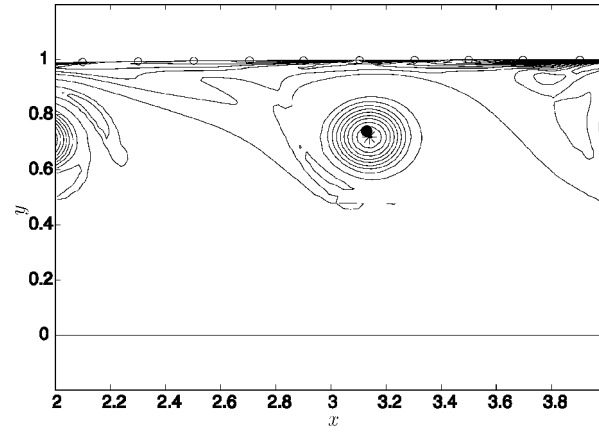

Fig. 6 Detected vortex position using the single-vortex algorithm with vorticity contours. The estimated circulation is $\Gamma = 0.759$ as opposed to $\Gamma = 0.909$ from DNS: ∗, vortex centroid. The rest of the notation is the same as in Fig. 5.

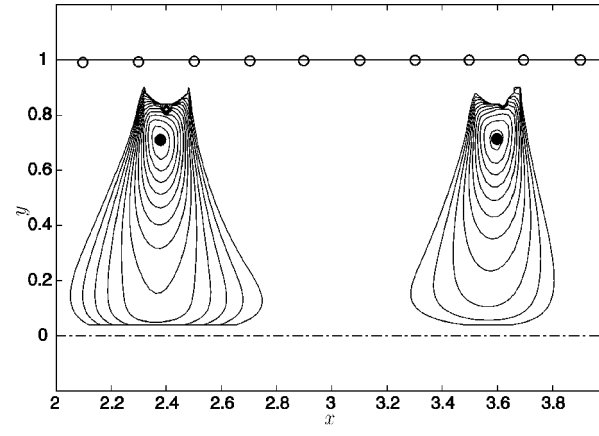

Fig. 7 Image map of two vortices created using the single-vortex algorithm. The corresponding vorticity contours are shown in Fig. 8. $J_{\min} = 1.007$ and 1.133 on the left- and right-hand sides, respectively. Notation is the same as in Fig. 5.

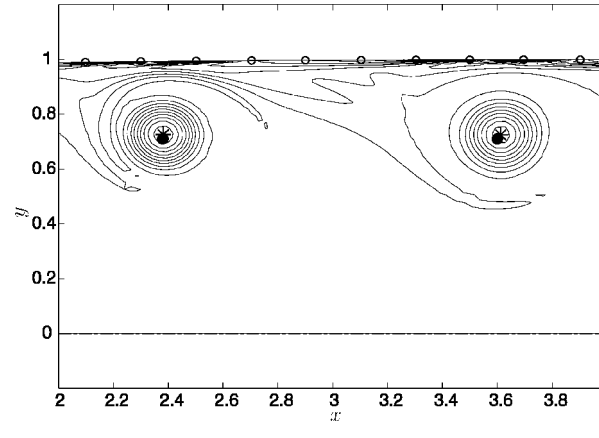

Fig. 8 Detected positions of two vortices using the single-vortex algorithm with vorticity contours. The estimated circulations are $\Gamma = 0.997$ and 0.995 as opposed to $\Gamma = 0.946$ and 0.889 for the left and right vortices, respectively. Notation is the same as in Fig. 6.

We also tabulate the standard deviations of the position and the circulation for each case in Table 1. Although the position tends to be predicted quite well (within 0.05 using 10 points), the accuracy of the circulation is relatively low (as much as 20%). Such a trend can be understood from the following analysis. For example, if a point vortex of $\Gamma = 1.0$ is located at $(x_0, y_0) = (3.0, 0.5)$ it gives $(\partial^2 J/\partial \Gamma^2, \partial^2 J/\partial x_0^2, \partial^2 J/\partial y_0^2) = (16.0, 67.9, 23.7)$ at the optimum point; namely, the resolution of Γ is several times as low as those

Table 1 Standard deviation of position and circulation

Case	Small vortex (5, 10, 20 points)[a]	Large vortex	Single-vortex algorithm[b]	Double-vortex algorithm[b]	Curved channel
$\sqrt{(\Delta x)^2}$	0.048, 0.015, 0.013	0.093	0.024, 0.172	0.014, 0.031	0.014
$\sqrt{(\Delta y)^2}$	0.104, 0.044, 0.037	0.138	0.041, 0.207	0.019, 0.049	0.057
$\sqrt{(\Delta\Gamma/\Gamma)^2}$	0.369, 0.191, 0.183	0.334	0.236, 0.749	0.107, 0.159	0.326

[a]Three values in the second column denote the values calculated using 5, 10, and 20 points, respectively.
[b] The fourth and fifth columns correspond to Figs. 18 and 19, and two values are for the right and left vortices, respectively. (The data were computed while two vortices were detected in the target domain.)

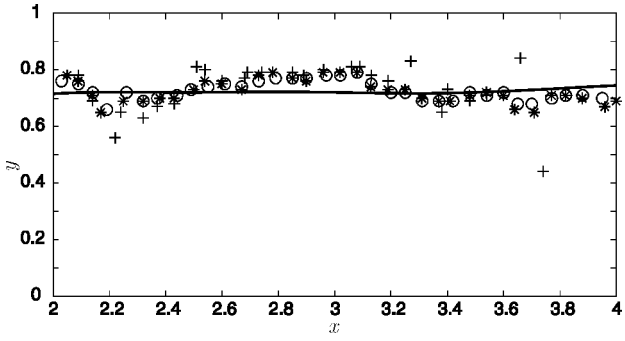

Fig. 9 Trajectory of a small vortex: ——, vortex centroid; +, detected positions from five observer points; ∗, those from 10 points; and○, those from 20 points.

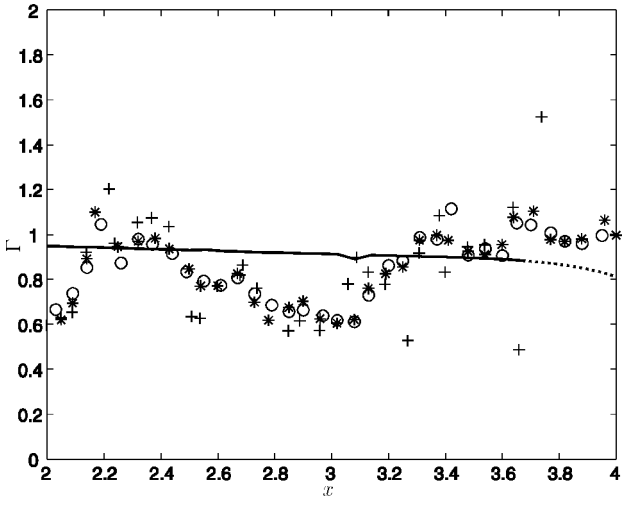

Fig. 10 Circulation change of a small vortex. Notation is the same as in Fig. 9. Dotted portion indicates that the leading edge of the vortex enters the computational sponge at the exit.

of x_0 and y_0. This also explains that the contour maps of $-J$ tend to be elongated in the y direction.

Figures 9 and 10 indicate that the deviations of detection are less sensitive to the number of the observer points if it is sufficient (say, more than 10 points in this example); namely, the error barely vanishes. They also indicate that the prediction deteriorates as the vortex exists near the inlet or the exit.

Figures 11–13 show the results for a larger vortex using 10 observer points. Compared with the preceding case, the discrepancies becomes larger. [The error in position is 0.17, and the circulation is 33% underestimated (see Table 1).] As the vortex spreads, the convective velocity deviates from a point vortex solution.[11] In this particular case a small counter-rotating vortex on the left-hand side might also enhance the error. It is less likely that the magnitude of circulation influences the accuracy because the signals are nearly linear in Γ^2, except for the terms of the ambient pressure p_∞ and the mean freestream velocity u_∞.

Figures 9, 10, 12, and 13 consistently show that as the position is mispredicted upward the circulation is underestimated, and vice versa. This tendency can be readily derived from the optimization process.

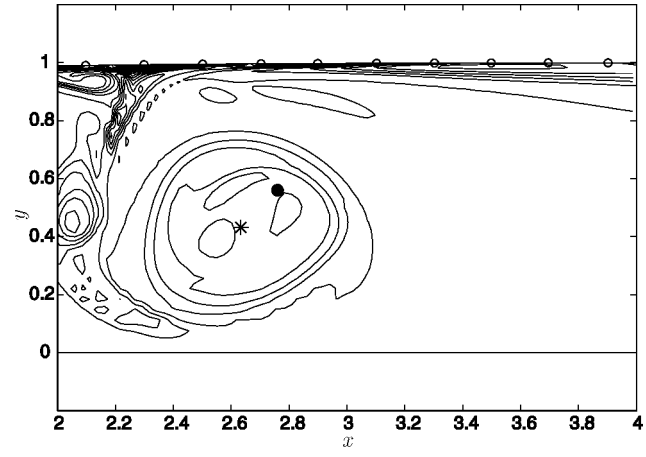

Fig. 11 Detected position of a large vortex using the single-vortex algorithm with vorticity contours. The estimated circulation is $\Gamma = 2.079$ as opposed to $\Gamma = 3.247$ from DNS. Notation is the same as in Fig. 6.

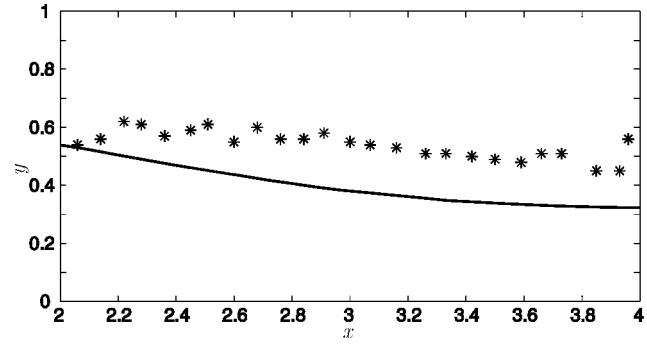

Fig. 12 Trajectory of a large vortex. Notation is the same as in Fig. 9 (detected from 10 points).

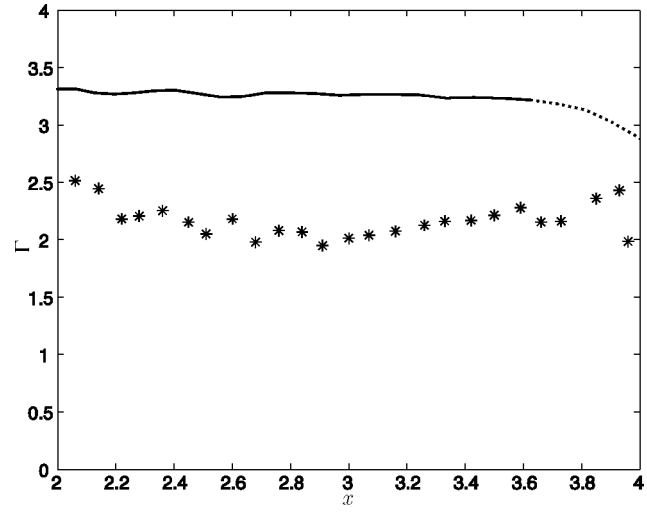

Fig. 13 Circulation change of a large vortex. Notation is the same as in Fig. 10.

B. Detection of Two Vortices

When we try to image two nearby vortices using the single-vortex algorithm, the accuracy of the detection becomes substantially worse, particularly for the one farther from the wall as shown in Figs. 14 and 15. By using the double-vortex algorithm, the accuracy is restored. Figure 16 shows the image map for the secondary vortex (the lower one) in which the position of the primary vortex (the higher one) optimizing the cost function is also plotted. As compared in Fig. 15, the accuracy of the detected positions is much improved, particularly for the secondary vortex (nearly five times better in terms of the standard deviation; see Table 1).

We found the algorithm optimizing the cost function with respect to four variables to be sensitive to the initial values. For example, in Fig. 16 the cost function converges when the initial value of circulation is in the range of $0.7\Gamma_2^* < \Gamma_2 < 1.7\Gamma_2^*$ with setting Γ_1, x_1, y_1 to be the optimum values, whereas in the single-vortex case (Fig. 5) it converges when $0.6\Gamma^* < \Gamma < 10\Gamma^*$. In fact, Fig. 16 indicates the region only where the cost function converges with one set of initial values that are close to the optimum values of Γ_1, x_1, y_1, and Γ_2. This numerical sensitivity can be reduced by increasing the number of the observer points. Figure 17 demonstrates that the one set of initial values converges over much wider area with 20 observers.

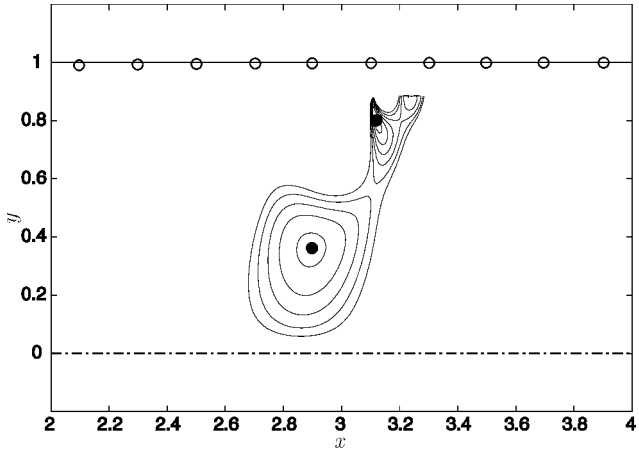

Fig. 14 Image map of two vortices created using the single-vortex algorithm (with 10 points). The corresponding vorticity contours are shown in Fig. 15. $J_{\min} = 1.152$ and 1.238 for the upper and lower vortices, respectively. Notation is the same as in Fig. 5.

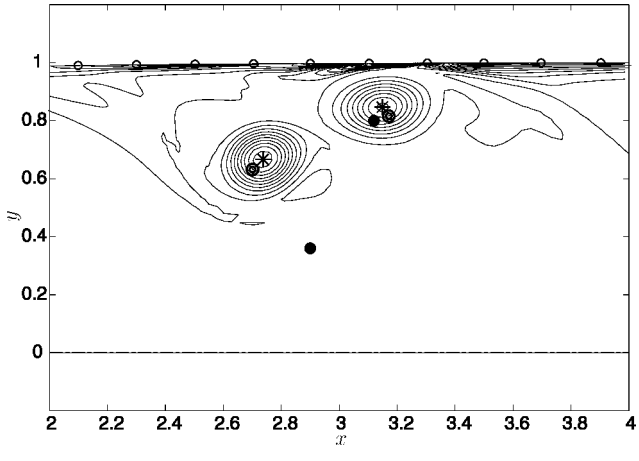

Fig. 15 Detected positions of two vortices with vorticity contours: ∗, vortex centroid; ●, position detected using the single-vortex algorithm; and◎, that using the double-vortex algorithm. The circulations computed from DNS are $\Gamma_1 = 0.737$ and $\Gamma_2 = 0.831$, those estimated using the single-vortex algorithm are $\Gamma_1 = 0.715$ and $\Gamma_2 = 1.611$, and those using the double-vortex algorithm are $\Gamma_1 = 0.707$ and $\Gamma_2 = 0.853$ for the upper and the lower vortices, respectively. The rest of the notation is the same as in Fig. 6.

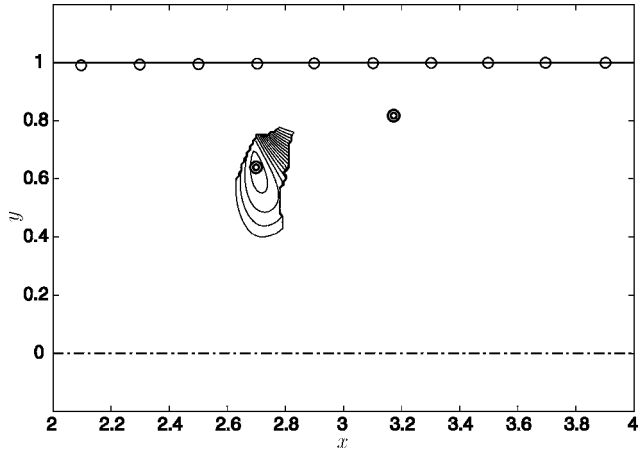

Fig. 16 Image map of the secondary vortex created using the double-vortex algorithm with 10 points. Contours of $-J$ are drawn ($J_{\min} = 0.1885$) with the interval of $\Delta J = 0.025$:◎, detected vortex positions. The rest of the notation is the same as in Fig. 5.

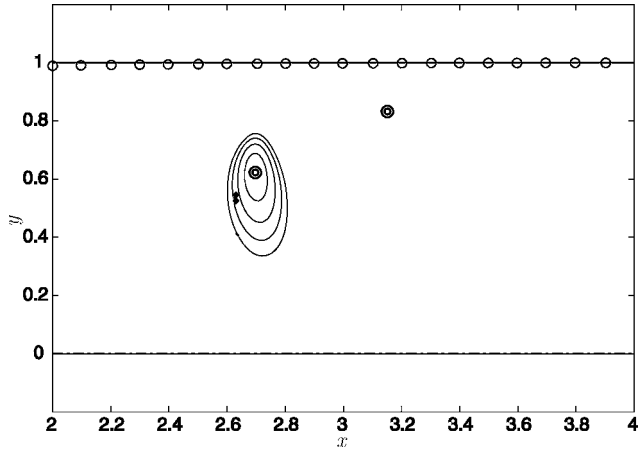

Fig. 17 Image map of the secondary vortex created using the double-vortex algorithm with 20 points. $J_{\min} = 0.0831$. Notation is the same as in Fig. 16.

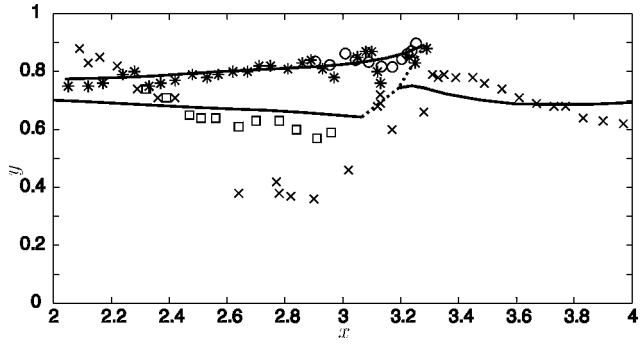

Fig. 18 Trajectories of two vortices: ——, vortex centroid (beyond the dotted lines, two vortices are indistinguishable because of pairing); ∗, ×, first and second (including the points after the pairing) vortices detected using the single-vortex algorithm, respectively; and○, □, those detected using the double-vortex algorithm. Ten points are used.

The range of convergence in the initial value of Γ_2 also increases as wide as $0.4\Gamma_2^* < \Gamma_2 < 4.4\Gamma_2^*$.

Figures 18 and 19 present the detected trajectories and the estimated circulations, respectively. They demonstrate that the double-vortex algorithm predicts the position of the lower vortex much more accurately, although both algorithms predict the higher one equally well. The double-vortex algorithm also estimates the circulation better (refer to Table 1 again). Once the vortices start to merge, neither

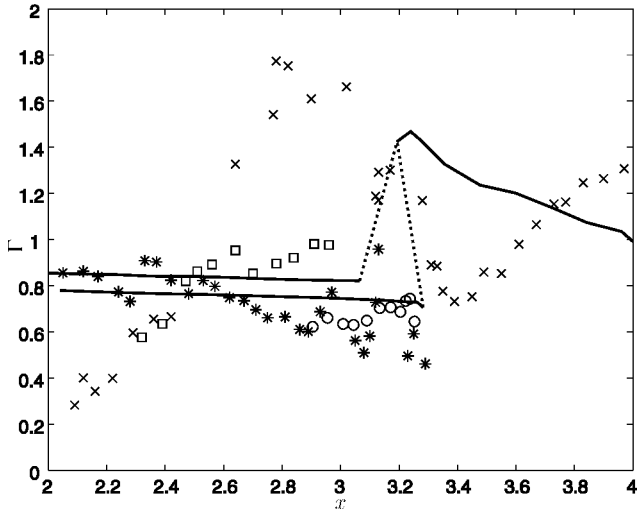

Fig. 19 Circulation change of two vortices. Notation is the same as in Fig. 18.

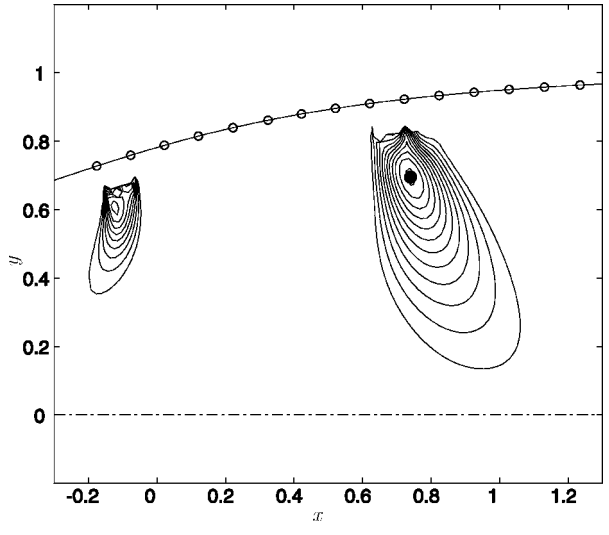

Fig. 20 Image map created based on an approximated solution in a curved channel (with 15 points). $J_{\min} = 1.218$. Notation is the same as in Fig. 5.

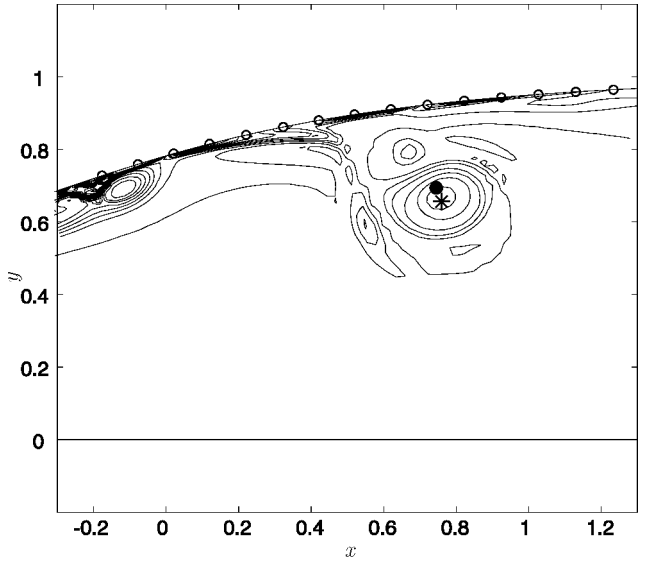

Fig. 21 Vorticity contour with the detected vortex position in a curved channel. The estimated circulation is $\Gamma = 0.684$, whereas that computed from DNS is $\Gamma = 1.035$. Notation is the same as in Fig. 6.

algorithm correctly distinguishes two vortices: the single-vortex algorithm indicates a single minimum of the cost function, and the double-vortex algorithm cannot find a local optimum point. Sufficiently far downstream, only one vortex is detected by the single-vortex algorithm, and the estimate of the circulation deteriorates. Note that one of the vortices is positioned close to the upstream end of the observer points ($x/h_2 \leq 2.3$); the double-vortex algorithm again cannot find a local optimum point. Thus, the double-vortex algorithm works well when both vortices are fully inside the observer array and their distance is somewhere in between 0.3–0.6.

C. Detection in a Curved Channel Based on an Approximated Function

Figures 20 and 21 depict the results from the curved-channel case. Although the ideal solution is only very approximate in this case, the algorithm captures the main vortex to nearly the same degree of accuracy (within 0.06 in position) as the straight-channel case. The small vortex growing near the separation point also appears on the map although the detected position is not accurate. Figure 22 depicts the comparison of the vortex trajectories and shows that the vertical coordinate tends to be estimated slightly higher (by 0.057 from Table 1) as also seen in the large vortex case (see Fig. 12). It also indicates that the algorithm becomes unstable when the vortex is too close to the separation point. Pressure on the wall near the separation point largely fluctuates depending on whether the boundary layer is attached or not. The magnitude of this fluctuation tends to exceed that of the pressure deficit induced by the vortex. Figure 23 shows that the circulation is underestimated by 33% (from

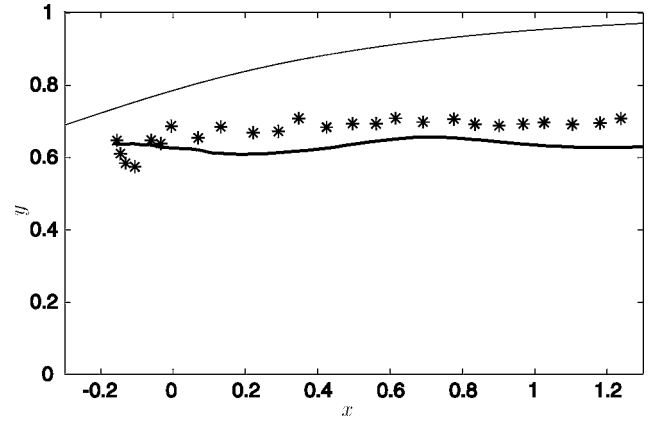

Fig. 22 Trajectory of a vortex in a curved channel. Notation is the same as in Fig. 9 (detected from 15 points).

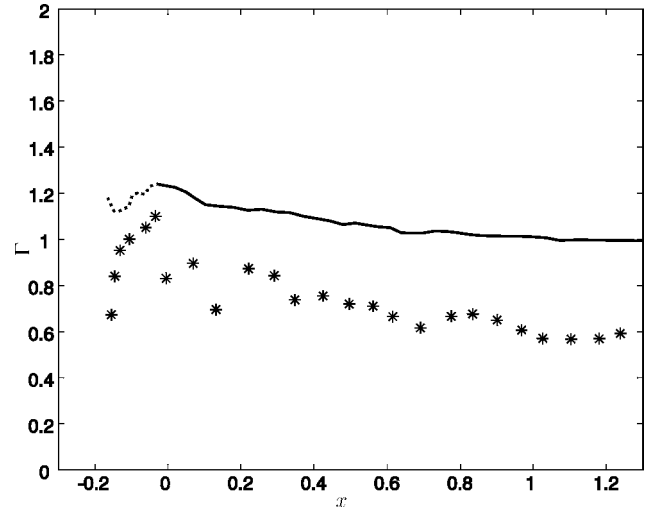

Fig. 23 Circulation change in a curved channel. Notation is the same as in Fig. 10: · · · · ·, the circulation cannot be well defined because the vortex is still attached to the boundary layer.

Table 1), although the decaying trend is qualitatively correct. Because the approximate solution is assumed proportional to a power of Γ as expressed in Eq. (12), the unsteady part of pressure cannot be appropriately represented by this expression.

D. Trajectories Processed Using Estimator-Corrector

Figure 24 compares the raw vortex trajectory and the one processed using the estimator-corrector for the small vortex case (the same case as in Fig. 9). Because the estimator-corrector includes the vortex dynamics, the trajectory becomes much smoother, and the deviation tends to decrease in time. Figure 25 compares the circulation change and shows similar trends although it starts with large deviation.

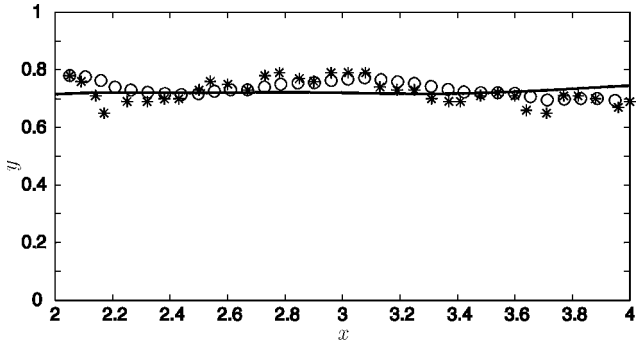

Fig. 24 Comparison of trajectories for a small vortex: ——, vortex centroid; ∗, regular algorithm; and○, with the estimator-corrector. Ten points are used.

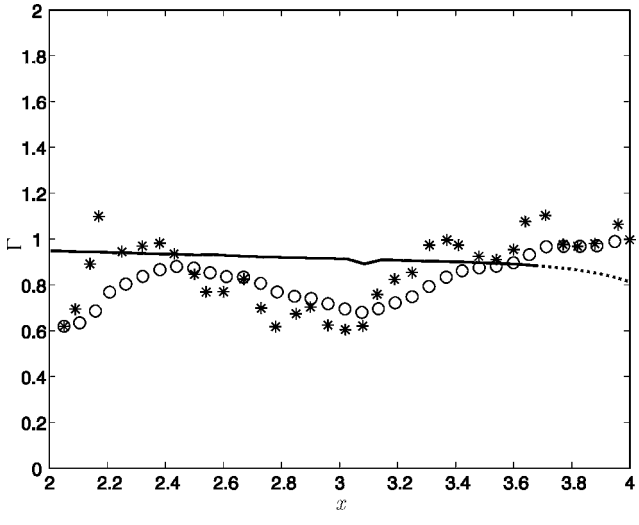

Fig. 25 Comparison of circulation change for a small vortex. Notation is the same as in Fig. 24.

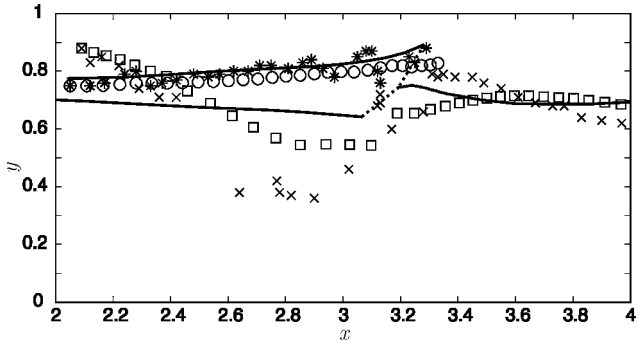

Fig. 26 Comparison of trajectories for two vortices: ——, vortex centroid; ∗, ×, first and second vortices detected using the regular single-vortex algorithm, respectively; and○, □, those detected using the single-vortex algorithm with the estimator-corrector. Ten points are used.

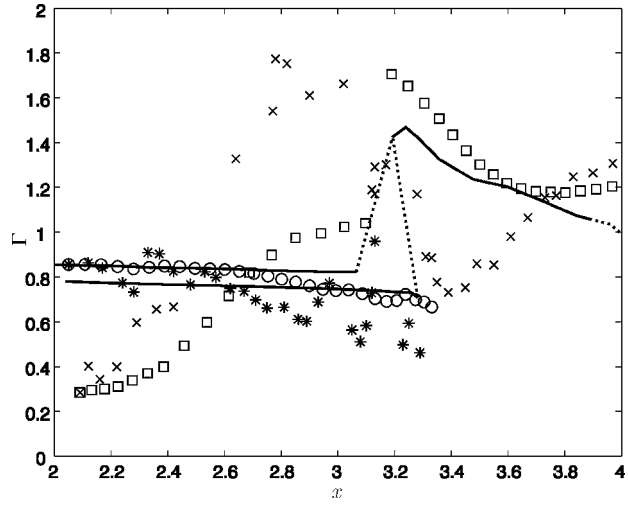

Fig. 27 Comparison of circulation change for two vortices. After vortex pairing the circulation is given by their summation and the position from their centroid. Notation is the same as in Fig. 26.

Figures 26 and 27 show the comparison for the two-vortex case. Even if we trace two vortices, the estimator-corrector can make the trajectories smoother and suppress the deviation toward downstream. However, its accuracy appears to be still less than that of the double-vortex algorithm shown in Figs. 18 and 19.

V. Conclusions

This paper has validated the capabilities of the inverse algorithms using a least-square cost function based on simple two-dimensional direct numerical simulation. We have demonstrated that the algorithms can detect one or two compact vortices. Not surprisingly, the accuracy of the detection depends on the suitability of the ideal solution P_k. We can improve this issue by introducing more parameters in a real problem. For example, we might be able to express a distributed vortex by introducing a core radius; consequently, we must optimize the cost function in terms of this parameter as well. On the other hand, the algorithm for multiple vortices indicates that finding the optimum parameters becomes more sensitive to the initial values as the number of the parameters increases.

To solve for more realistic flowfields, the algorithm requires further improvement; namely, we must find a simple expression for the ideal solution and develop a stable and fast optimization algorithm for multisolutions. For example, if we apply this algorithm in three dimensions using the solution for a line vortex, the resultant image map can capture large-scale line vortices with small curvatures. However, when the flow is more complex we might need to include additional parameters for curvature or to consider instead vortex rings. The additional complexity will require a relaxation technique for optimization in addition to the estimator-corrector. Moreover, if noise levels from small-scale turbulence in the boundary layer become comparable to signals from the large-scale structures away from the wall, the measurement using surface pressure will likely fail.

In addition to vortical flows, we might be able to apply such a general inverse algorithm in many applications. In particular, active flow control techniques suffer from obtaining reduced-order representations of the flowfields. Flow reconstruction techniques, such as the proper orthogonal decomposition[4] or the stochastic estimation,[5] can characterize complex unsteady flow patterns; however, they require the information of the entire flowfield in most cases. In contrast, when the key structures of the flowfield are somewhat known this inverse algorithm can reconstruct an approximate flowfield only from the information on the boundary. The key to successfully solve the problem is the choice of the observer points and the measured quantities as well as the suitability of the ideal solution.

Acknowledgments

This research was supported in part by the DARPA (Defense Advanced Research Projects Agency) program (Contract

F49620-00-C-0035). We thank Richard Murray for an idea of the estimator-corrector and Kazuo Sone for generating several files.

References

[1]Derou, D., Dinten, J.-M., Herault, L., and Niez, J.-J., "Physical-Model Based Reconstruction of the Global Instantaneous Velocity Field from Velocity Measurement at a Few Points," *Proceedings of the Workshop on Physics-Based Modeling in Computer Vision*, IEEE Computer Society Press, Los Alamitos, CA, 1995, pp. 63–69.

[2]Gumerov, N. A., and Chahine, G. L., "An Inverse Method for the Acoustic Detection, Localization and Determination of the Shape Evolution of a Bubble," *Inverse Problems*, Vol. 16, 2000, pp. 1741–1760.

[3]Bonnet, J. P., Delville, J., Glauser, M. N., Antonia, R. A., Bisset, D. K., Cole, D. R., Fiedler, H. E., Garem, J. H., Hilberg, D., Jeong, J., Kevlahan, N. K. R., Ukeiley, L. S., and Vincendeau, E., "Collaborative Testing of Eddy Structure Identification Methods in Free Turbulent Shear Flows," *Experiments in Fluids*, Vol. 25, 1998, pp. 197–225.

[4]Lumley, J. L., *Stochastic Tools in Turbulence*, Academic Press, New York, 1970, Chap. 3.

[5]Adrian, R. J., and Moin, P., "Stochastic Estimation of Organized Turbulent Structure: Homogeneous Shear Flow," *Journal of Fluid Mechanics*, Vol. 190, 1988, pp. 531–559.

[6]Chang, P. A., Piomelli, U., and Blake, W. K., "Relationship Between Wall Pressure and Velocity-Field Sources," *Physics of Fluids*, Vol. 11, No. 11, 1999, pp. 3434–3448.

[7]Naguib, A. M., Wark, C. E., and Juckenhöfel, O., "Stochastic Estimation and Flow Sources Associated with Surface Pressure Events in a Turbulent Boundary Layer," *Physics of Fluids*, Vol. 13, No. 9, 2001, pp. 2611–2626.

[8]Murray, N. E., and Ukeiley, L. S., "Estimation of the Flowfield from Surface Pressure Measurements in an Open Cavity," *AIAA Journal*, Vol. 41, No. 5, 2003, pp. 969–972.

[9]Saffman, P. G., *Vortex Dynamics*, Cambridge Univ. Press, New York, 1992, pp. 119–122.

[10]Suzuki, T., Colonius, T., and Pirozzoli, S., "Two-Dimensional Diffuser Model for Vortex Shedding and DNS Study on Periodic Separation Control," *Journal of Fluid Mechanics* (submitted for publication).

[11]Pierrehumbert, R. T., "A Family of Steady, Translating Vortex Pairs with Distributed Vorticity," *Journal of Fluid Mechanics*, Vol. 99, Pt. 1, 1980, pp. 129–144.

A. Karagozian
Associate Editor